Optical properties of the dibenzothiazolylphenol molecular crystals through ONIOM calculations: the effect of the electrostatic embedding scheme

Optical properties of the dibenzothiazolylphenol molecular crystals through ONIOM calculations: the effect of the electrostatic embedding scheme.

Davide Presti[1],* Alfonso Pedone[1],' Ilaria Ciofini[2], Fréderic Labat[2], Maria Cristina Menziani[1] and Carlo Adamo[2,3]

[1]*Dipartimento di Scienze Chimiche e Geologiche, Università di Modena e Reggio-Emilia, via G. Campi 103, I-41125 Modena, Italy.*

[2]*Institut de Recherche de Chimie Paris CNRS Chimie ParisTech, 11 rue P. et M. Curie, F-75005 Paris 05, France.*

[3]*Institut Universitaire de France, 103 Boulevard Saint Michel, F-75005 Paris, France.*

Corresponding Author

Dr. Davide Presti,

Department of Chemical and Geological Sciences,

University of Modena and Reggio Emilia, via G. Campi 103, Modena, 41125, Italy.

E-mail: davide.presti@unimore.it;

Abstract

Periodic Density Functional Theory and hybrid ONIOM time-dependent DFT/MM cluster calculations have been carried out to investigate the ground and excited state properties of the crystalline structures of the enolic and ketonic tautomeric forms of a propoxy-substituted dibenzothiazolylphenol molecule (**OPr**), a prototype for systems undergoing to the excited state intramolecular proton transfer process.

The crystalline structures of the tautomeric forms are well reproduced and, as expected, at the ground state the enol polymorph is predicted to be more stable than the keto one. At the excited state, the effect of the environment on time-dependent DFT calculations has been accounted for by including a charge embedding scheme, and the influence of different kinds of point charges (Mulliken, CM5, RESP and Q_{Eq}) in determining the optical properties of the central molecule has been investigated.

The results reveal that, in fair agreement with experimental data, the absorption (emission) energies of the enol (keto) **OPr** molecule is red shifted of about 3 (3) nm going from the gas phase to chloroform and blue shifted of 10 (23) nm going from the gas to the crystal phase when the electronic embedding with Mulliken charges is employed. The electrostatic embedding influence the excited state properties more severely than the ground state and, apart the Q_{Eq} charges, all other models provide Stokes' shifts in reasonable agreement with experimental data.

Keywords : ESIPT fluorophores, molecular crystals, TD-DFT, ONIOM, electrostatic embedding

1. Introduction

In the last years, molecular solids have found a large growth in applications as optic materials with versatile uses in photochemical science and engineering.[1]

Several organic molecules exhibiting *charge transfer* (CT) and/or Excite-State Intramolecular Proton Transfer (ESIPT) processes after irradiation have shown interesting photo-chromic properties when arranged in the solid state.[2–5]

Recently, Sakai et al.[6] synthesized and characterized (by X-Ray Diffraction and UV-Visible absorption and fluorescence spectroscopy) four different alcoxy-substituted (metoxy-, ethoxy-, propoxy- and butoxy-) dibenzothiazolylphenol molecular crystals that exhibit strong ESIPT fluorescence.

Figure 1 reports the chemical structures of the enolic and ketonic forms of the propoxy-substituted compound (hereafter named **OPr**) as well as the photochemical mechanism responsible of its luminescent properties.

This chromic compound shows, both in solution (chloroform solvent) and in solid-state, an orange-red fluorescent emission, that in the crystal gives rise to a remarkable fluorescent quantum yield (Φ_{FL} = 0.38). The proposed photophysical molecular mechanism involves: i) the photoirradiation of the enol tautomeric form of **OPr**, followed by ii) an ESIPT process that leads to the fluorescent keto tautomer. The spectral differences observed in solid-state fluorescence (not sizeable in the molecular case) for diverse substitutions of the alcoxy- group were explained[6] making use of the Davydov exciton coupling theory.[7] Two systems (**OPr** and the metoxy-substituted one, **OMe**) form H-aggregates, whereas the other two systems (propoxy- and butoxy-substituted) form J-aggregates. The stacked molecular displacement of molecules within the crystal, originates a face-to-face (head to tail) coulomb interaction between the molecular transition dipole moments that for H-aggregates (J-aggregates) yields to a batochromic

(hypsochromic) shifted emission with respect to the non-substituted compound. Therefore, the emissive lowest singlet excited state is destabilized (overstabilized) depending on the competing dipole-dipole interactions.

Such experimental observations were partially supported[6] only for **OMe**, with a Density Functional Theory (DFT) computation in gas-phase of HOMO-LUMO frontier orbitals of the two tautomers at the ground state geometry. These calculations, however, did not provide much theoretical information on the optical properties of **OMe** and, more in general, on this family of red fluorophores, since excited states were not examined. Moreover, environmental effects mimicking the solvent (chloroform) and/or the solid material were not considered.

The aim of the present work is to provide theoretical insights into the chromic properties of such family of solid compounds through the study of the **OPr** system (for which the experimental enol structure is available), utilizing a computational protocol based on a quantum mechanical (QM) periodic approach coupled with ONIOM QM/MM cluster calculations.[8] The results obtained will allow the assessment of the efficiency of such protocols for ESIPT molecular crystalline materials as **OPr**, and the derivation of useful indications for future theoretical modelling of solid state fluorophores.

In fact, although the photophysical/photochemical properties of molecular crystals attracted a great interest,[9–11] their computational characterization is still in a germinal stage. This is mainly due to the cost/accuracy ratio of time-dependent techniques needed for the study of very large systems. Moreover, the complexity of molecular phenomena of interest are unavoidably combined with the notorious lacks of standard quantum methods (e.g. DFT) in describing non-classical long-range effects implicitly.[12–14] These lacks, in DFT, have partly been solved with the introduction of the *a posteriori* correction schemes to recover dispersive interactions.[14]

In order to define a feasible approach for describing large solid systems, i.e. a good ratio between computational cost and accuracy, Density Functional Theory – coupled with the *a posteriori* dispersion correction[15, 16] – has been adopted to model the crystalline ground-state structures. Linear response (LR) time-dependent DFT (TD-DFT), within the frame of multiscale ONIOM QM/MM cluster calculations, has been chosen to investigate the UV-Visible absorption and emission optical properties from the excited states of **OPr**, and the results have been compared with standard TD computations on gas-phase and solvated monomers.

Finally, since the effect of the environment during the TD-DFT calculations have been accounted for by using the ONIOM approach,[17, 18] we have investigated the influence of different kinds of point charges (to describe the low level region) in determining the optical properties of the central molecule.

The paper is organized as follows: computational details are given in Section 2; ground-state structural properties of the system are commented in Section 3.1, whereas inter- and intramolecular parameters are discussed in Sections 3.2 and 3.3. The main results on the UV-Visible optical properties of **OPr** are exposed and commented in Section 3.4. The role played by charge embedding in this context is analyzed in Section 3.5. Then some general conclusions and future directions are drawn.

2. Computational Details

2.1 Ground state periodic calculations. Full structural relaxations of the ground state forms of the enol- and keto- polymorphs of **OPr**[6] were carried out at the B3LYP-D*/6-31G(d,p) level[16, 19] using a parallel version of the CRYSTAL09[20, 21] suite of programs. This setting has proved quite accurate in describing the structural properties of molecular crystals.[22, 23]

The performance of the 6-31G(d,p) basis-set was checked against richer basis-sets including diffuse functions (6-31+G(d,p), 6-311+G(d,p))[24, 25]. The results, which are reported in the Supporting Information, revealed that the addition of both ζ-valence and diffuse functions affects negligibly the ground state structures.

A full use of symmetry and periodic boundary conditions (PBC) was imposed, as implemented in CRYSTAL09. The Monkhorst-Pack grid was set to 4 4 (see keyword SHRINK),[21] that in the case of **OPr** corresponds to 30 *k*-points within the Irreducible Brillouin's Zone. The eigenvalues level shift was locked to 1 a.u. (LEVSHIFT 10 1), and the thresholds on the convergence of bielectronic integrals tightened (TOLINTEG 7 7 7 9 18) with respect to default values.

The starting structure of the enol form of **OPr** is the one experimentally resolved by Sakai et al.[6] The structure of the metastable keto polymorph is not known but the same crystal symmetry of the enol form ($P2_1/c$ space group) was imposed. Therefore, we manually moved the hydrogen involved in the ESIPT process from oxygen to nitrogen and optimized the keto form obtained, keeping the same computational conditions as for the enol polymorph (only the α and γ parameters were constrained at 90). As a structural check, a symmetry operator search with a tolerance of 0.01 Å (making use of Accelrys Materials Studio Visualizer, ver. 6.0) on the *P1* cell of the optimized keto polymorph revealed that the crystal maintained the same symmetry. This is probably the consequence of the large size of the **OPr** molecules, which with their quasi-planar geometry and the presence of π-stacking interactions and the consequent crystal packing (see **Figures 2** and **3**), impede possible rotations and other structural changes.

2.2 Monomer calculations. The ground state of the molecular enol- and keto- forms of **OPr** were optimized employing the B3LYP[19] density functional approximation.

Calculations were carried out in gas-phase and in solution: according to the experimental measurements carried out in chloroform ($CHCl_3$), a Conductor-like Polarizable Continuum implicit model of solvation[26] (C-PCM) was used to describe $CHCl_3$.

Excited state properties were computed at the same level of theory as for ground-state, adopting the 6-31+G(d,p) basis-set. The addition of diffuse functions was necessary for a better description of the excited-states. As mentioned before, these are not crucial for the structural properties in the ground state: in the latter case the 6-31G(d,p) basis-set was used also for monomers, for coherence with PBC calculations.

Vertical excitation energies (UV-Visible absorption) were calculated both for the enol and keto forms (the first ten states have been considered), whereas the full optimization of the first excited singlet, S_1 (UV-Visible emission), was performed only for the keto form, since this latter is the responsible for the main fluorescent emission of **OPr** both in solution and in solid-state. All calculations on monomers and clusters (except for charge embedding, *vide infra*) were carried out with the Gaussian09 (Rev. D.01) program package.[27]

2.3 QM/QM' cluster calculations. Inspired by a theoretical protocol discussed elsewhere,[8] to mimic and predict the photophysical features of **OPr** in solid-state we extracted, from the fully optimized enol and keto crystalline structures, two clusters of molecules that in the following will be referred to as **C-OPr-enol** and **C-OPr-keto**, respectively. These both contain 17 **OPr** molecules (799 atoms, 47 atoms/molecule) in their enol (keto) form. The size of clusters was chosen in order to include explicitly a surrounding molecular environment of 16 molecules/752 atoms (set as low-level region), i.e. a "cage" that is responsible of the main noncovalent interactions affecting the central molecule of **OPr** (set as high-level region).

Then, the central **OPr** molecule (i.e. the high-level region) of **C-OPr-enol** and **C-OPr-keto** was further optimized without symmetry constraints, within an ONIOM-like[17, 18] QM/QM' cluster

approach in the framework of mechanical embedding. The B3LYP/6-31G(d,p) level of theory was employed for the QM region, while the Hartree-Fock (HF)/STO-3G method was employed for the QM' region, whose geometry was maintained fixed at its crystalline structure.

Excited state properties (vertical UV-Visible absorption and emission) have been computed at the QM/QM' level with the same methods. The 6-31+G(d,p) basis-set was used for the high-level QM region. The fluorescence properties were obtained by optimizing the first bright excited state (S_1, singlet), keeping the central molecule of the keto form of **OPr** spatially unconstrained within the fixed environment region.

The simulated UV-Visible spectra were plotted through an in-house code as gaussian convolutions of the computed main vertical transitions, using a full-width at half maximum (FWHM) of 0.1 eV. Intensities were normalized to 1 a.u.

2.4 Charge model effects on cluster calculations results. The effect of the charge model on the UV-Visible optical properties of clusters were studied by means of TD-DFT/MM single-point energy calculations coupled with an electrostatic embedding (EE) scheme (involving explicit charges for the low level system) applied to the ground and excited geometries of the **OPr** central molecule optimized at the B3LYP/HF level with mechanical embedding.

The calculations were carried out by using ground state charges for the low level region. The Mulliken,[28] CM5,[29] RESP,[30][31] and Q_{Eq}[32] charges were tested. The Mulliken charges have been computed at the HF level by using the STO-3G basis set, since it has been demonstrated to provide good charges (even if for error cancellation).[33]

CM5 type charges were computed at the HF/6-31G(d) level and RESP charges were computed at the HF/STO-3G and HF/6-31G(d).

Frontier orbitals were depicted with an isosurface density value of 0.02 a.u. for **OPr** in gas-phase, solution and (for the central molecules of) cluster systems.

3. Results and Discussion

3.1. Ground state polymorphs. The stable crystalline enol polymorph of **OPr** is characterized by the presence of 4 molecules (Z=4) within the unit cell (188 atoms/cell), that belongs to the $P2_1/c$ monoclinic space group. The B3LYP-D*/6-31G(d) fully optimized (atomic positions and lattice parameters) structure is pictorially represented in **Figure 2**, and compared with the fully optimized keto structure (additional images of the unit cell are reported in the Supporting Information). It can be noted that the two polymorphs are very similar, because of the same crystalline symmetry. The keto form, however, is slightly more closely packed than the enol one, as confirmed by the differences in cell parameters, reported in **Table 1**.

As regards the prediction of cell parameters with respect to experiment (enol form), small deviations are furnished by B3LYP-D* (**Table 1**), except for the angle β (-1.676°) that is more severely underestimated. This is probably due to the presence of dispersive interactions originated by π-π stacking patterns between molecules, located along a diagonal vector in the *ac* plane. However, the total Relative Deviation % on the unit cell volume (RD %, obtained as [Volume(calc.) - Volume(exp.)] / Volume(exp.) x 100) is smaller than 5% (-4.40%). It has to be recalled, however, that cell volumes are only qualitatively comparable due to thermal effects, the experimental enol structure being determined at 100 K.

As for the keto polymorph, the RD % on volume amounts at -0.86%, the major contributions to this deviation being the shortening of the lattice constant b (-0.170 Å) and the shrinking of the angle β (-0.576°).

Table 1 also reports the theoretical relative stability, obtained as difference between the keto and enol total ground state energies. As expected, the fully optimized enol polymorph is predicted to be more stable than the fully optimized keto one, of about 19 kcal/mol. The difference per molecule (ca. 5 kcal/mol) is larger than what can be expected (1-2 kcal/mol) for crystalline phases owing such structural similarity. Nonetheless, one should remember that the hydrogen atom involved in the ESIPT undergoes to a notable displacement from the enol to the keto form (see below, Section 3.2).

3.2. Crystals vs. Clusters: intermolecular interactions. The **C-OPr-enol** and **C-OPr-keto** clusters were extracted from the fully optimized crystals, as described in Section 2.4. We recall that the B3LYP was employed for the subsequent ground state optimization of the central enol/keto molecule of **OPr** (high-level region) within the fixed environment of 16 surrounding molecules (low-level region) treated with HF/STO-3G.

As first step in the comparison between crystalline and cluster forms of **OPr**, *inter*molecular distances have been considered. Selected parameters (among all possible ones included within a range of 4 Å around the central molecule) are listed in **Table 2,** and shown in **Figure 3** (bottom), together with atom labels, for the enol tautomer (see Figure S.2 of the Supporting Information for the keto tautomer).

It should be noticed that the distances C16···H(a') and H(a)···C16 are equivalent by symmetry, as proven by their equal values observed in solid-state (2.735 Å enol form; 3.586 Å keto form). When the central molecule is optimized within a fixed environment such symmetry is broken, therefore for clusters, the two distances are not equivalent. In particular, the optimized configuration of **C-OPr-enol** leads to a very small deviation for C16···H(a') (+0.008 Å), while H(a)···C16 remains the same (3.586 Å). For **C-OPr-keto**, instead, a larger deviation is observed

for C16···H(a') (-0.044 Å); a small one is obtained for H(a)···C16 (+0.008 Å). For the other distances, absolute deviations within 0.0058 Å are given, the larger ones involving hydrogen atoms. Instead, the measured π-π stacking distance remains very similar for the two tautomers, in solid state and clusters (ca. 3.650 Å). This is ascribable to the fact that molecular flexibility is impeded by the packing of central **OPr** within its environment.

3.3. Intramolecular parameters: crystals, clusters and monomers. The comparison between **OPr** structures in different states of aggregation is important for a better understanding of the optical properties analyzed in the next Sections. In this case, only *intra*molecular parameters can be compared. These, however, in both crystals and clusters also reflect the spatial displacements due to intermolecular interactions. In principle, one should expect some relevant differences between structures, because monomers in gas phase and in solution have a major number of degrees of freedom. In crystals, instead, covalent and noncovalent parameters are deeply interdependent, but constrained to the whole crystal symmetry. Finally, clusters depend on their starting crystalline geometry, at which the external molecules are fixed; the central **OPr** molecule, nonetheless, experiences some degree of motion, which is mechanically limited by its inclusion in the environment.

Probably, as a consequence of the mild changes of the intermolecular parameters discussed above, also the intramolecular ones – a subset of those given in Table S.1 is reported in Table S.2 of the Supporting Information, for the enol tautomer – do not present severe variations between the different states of aggregation of **OPr**. This is true also when comparing the gas-phase monomer with the corresponding crystal polymorph: in fact, the gas-phase **OPr** molecule presents a planar conformation, for which rotations of dihedral angles are negligible – and thus not reported. As expected, the parameters which show more substantial variations correspond to

those related to the intramolecular hydrogen bond (see deviations of O1–H 0.16/0.18 Å; and H···N1 -0.14/-0.18 Å in Table S.2), especially the angle O1–H–N1 (-4.1° optimized crystal to -5.7° gas-phase). Nonetheless, this parameter is exposed to marked variations for negligible changes in the displacement of the hydrogen atom.

An interesting aspect is the difference between the ground state optimized geometry (S_0) of the keto tautomer and its excited singlet state (S_1) optimized geometry, the latter corresponding to the optical fluorescent moiety. The related inter- and intra- molecular parameters are compared in **Table 3**, and the difference between distances of selected intra- and intermolecular parameters for the **OPr** keto tautomer are given in **Figure 4.**

Importantly, the structural variation between S_1 and S_0 have similar extent, and the same sign independently from the system considered. Looking at H-bond parameters, it is reasonable to suppose that the ESIPT mechanism, which is nonetheless of intramolecular nature, is actually transferable from the singly molecular (gas- or solvated-) phase to the (cluster representation of the) solid-state, at least from a purely structural point of view.

Figure 4 shows that the distances related to the H-bond present larger variations when going from S_1 to S_0 (ex.: N1···O1 +0.11/+0.12 Å and O1···H +0.21/+0.22 Å), highlighting the rise of a mild repulsion between the H-bond acceptor species (O1) and both the donor species (N1) and the H atom. This could represent a stabilization of the keto-imine group, going towards the excited S_1 minimum from the vertically excited S_0 geometry. The covalent H–N1 bond, instead, remains almost unaltered (deviation -0.03 Å).

Differences in the intermolecular parameters defined before for the enol form (see **Figure 3**), are reported for the **C-OPr-keto** cluster. All such differences are extremely tiny, falling all within 0.08 Å. The larger ones involve the intermolecular O1···H(c) and O2···H(d) distances (of -0.057 Å and +0.056 Å, respectively).

3.4 Optical properties: gas, solution and clusters. The vertical excitation and emission energies of **OPr** molecule in the gas phase, in chloroform and in the crystal are summarized in **Table 4**.

Figure 5 reports both the absorption and the emission spectra obtained from the computed main TD-B3LYP/6-31+G(d) vertical transitions of gas-phase, solvent ($CHCl_3$) and cluster (TD-B3LYP/6-31+G(d):MM with embedding of HF/STO-3G Mulliken charges). We recall that the emission spectrum was calculated only for the keto tautomer, since it is the fluorescent system. The absorption spectrum, on the other hand, corresponds to the enol tautomer, the most stable form at the ground state.

The results reveal that the vertical excitation energy (VEE) of the enol form of **OPr** is red shifted of about 3 nm going from the gas phase to chloroform and blue shifted of 10 nm when going from the gas phase to the crystal phase here simulated by the cluster with electronic embedding using Mulliken charges.

The same behavior is observed for the emission energy, that is, the emission of **OPr** in solution is red shifted of 3 nm with respect to what computed in the gas phase, whereas the emission of **OPr** in the crystal is blue shifted of 23 nm when the Mulliken EE is used. The absorption and emission energies computed for the molecule at the crystal structure without electronic embedding are also very similar to those computed in vacuum confirming that the structural changes between the two aggregation states are minimal.

As expected, also the vertical energies computed using the implicit solvation model are very similar to those computed in the gas-phase, due to the relatively low dielectric constant of chloroform.

Regarding the comparison with experimental data, predictions are in fair agreement with the available data,[6] discrepancies being within 0.1-0.2 eV. The full experimental absorption

spectrum ($\lambda_{max,abs}$ = 390 nm) is available only for the compound in solution whereas for the crystalline form only the maximum in the excitation spectra is available ($\lambda_{max,exc}$ = 438 nm).

It is interesting to note that the blue shift (30 nm) observed in the experimental fluorescent spectra of **OPr** crystal (λ_{exc} = 589 nm) with respect to chloroform (λ_{exc} = 619 nm) is well reproduced by our calculations. In fact, B3LYP/MM EE (Mulliken) calculations (λ_{exc} = 563 nm) provide a blue shift of 28 nm with respect to chloroform (λ_{exc} = 591 nm).

Overall, B3LYP results are very good. The frontier orbitals, depicted in **Figure 6** (and in Figures S.3-S.8 of Supporting Information) clearly show that the HOMO-LUMO excitation possesses a partial CT character, more marked for the keto tautomer when using the optimized S_1 geometry. It is worth to note that the B3LYP functional provided consistent results due to the limited through-space character associated to these transitions. More importantly, the ESIPT feature of the **OPr** system becomes noticeable when comparing the frontier orbtitals of the enol tautomer, where the density is delocalized over the whole molecule (except for the propoxy- group) and the frontier orbitals of the keto tautomer, where a charge depletion arises, in turn, on the two lateral aromatic groups.

3.5 The effect of charges on the optical properties OPr in the solid state. **Figure 7** reports the UV-Visible spectra obtained from cluster calculations using different sets of charges in the low level region. We recall that, in order to separate structural and electronic effects on the optical properties, cluster calculations were performed using both S_0 and S_1 structures (obtained without electronic embedding at the TD-B3LYP/6-31+G(d):HF/STO-3G level).

Figure 7 shows that the absorption region is overall less relevant than the emission region, as all the methods furnish a very similar λ_{max}, with a maximal variation of 20 nm, evident from the inset of the figure. Such differences fall within the limit of accuracy of the TD-DFT method used.

The slight differences observed for peaks positions are, however, in agreement with the trend reported for the emission of the **C-OPr-keto** clusters, for which more marked variations in $\lambda_{max,emi}$ are observed. This underlines the fact that electronic effects influence the excited state properties more severely than those of the ground state.

With respect to the experimental emission maximum in solid state ($\lambda_{max,emi}$ = 589 nm), the TD-B3LYP/HF keto emission without embedding (orange dashes) is redshifted ($\lambda_{max,emi}$ = 605 nm), whereas the method adopting the electronic embedding (i.e. TD-B3LYP/MM EE, green dashes) features an opposite trend, i.e. a blueshift ($\lambda_{max,emi}$ = 563 nm). The difference between these two values is relevant, and shows how the electronic embedding obtained using the HF/STO-3G Mulliken charges induces an hypsochromic shift of the emission band.

The spectra obtained at the TD-B3LYP/MM level with RESP charges computed at the HF/STO-3G and HF/6-31G(d) are, indeed, mildly distinguishable (pink and violet dashes, respectively). The robust formulation of such model of charges furnishes a $\lambda_{max,emi}$ of 591 nm (STO-3G), and a $\lambda_{max,emi}$ of 590 nm (6-31G(d)) that are significantly in better agreement with experiment, and rather independent from the basis-set size. Though the minimal STO-3G basis-set is generally discouraged to compute most properties for obvious reasons, it represents an interesting option, especially from the point of view of the computational cost, in the perspective of being used to calculate low-level charges for multiscale simulations.

CM5 charges also provide a nice prediction ($\lambda_{max,emi}$ = 579 nm) of the experimental emission wavelength in solid state, showing a spectral profile that mostly coincides with those furnished by the RESP model.

The Q_{Eq} charges, instead, furnishes a marked redshift (+41 nm, $\lambda_{max,emi}$ = 630 nm), compared to experiment and to the other charge models tested.

Finally, another more important property that can be employed to evaluate the effect of embedded charges, is the variation that refers to the experimental Stokes' shift which is 151 nm. **Table 5** reports the Stokes' shift computed with different charges. Apart the Q_{Eq} charges, all the other sets of charges provide small deviations from the experimental one, with Mulliken charges yielding the best results.

Conclusions

The absorption and emission energies of the **OPr** molecule in gas phase, in solution and crystalline state have been investigated.

The absorption and emission spectra of the **OPr** molecule in the crystal have been computed by using a protocol involving hybrid QM/MM ONIOM cluster calculations with the inclusion of electrostatic embedding effects.

We have shown that the description of excited states depends crucially on the model adopted to compute charges in the low level region (Mulliken, CM5, RESP and Q_{Eq} model charges have been compared).

In fair agreement with experimental data, the absorption (emission) energies of the enol (keto) **OPr** molecule is red shifted of about 3 (3) nm passing from the gas phase to chloroform and blue shifted of 10 (23) nm passing from the gas to the crystal phase when the Mulliken charges are employed. The Stokes' shift are also in reasonable agreement with experimental data apart for the calculation employing the Q_{Eq} charges.

Acknowledgements

H. P. Hratchian and M. J. Frisch are kindly acknowledged. Computational resources for this work were granted by 'Project 100339' (2013-2014) at GENCI-IDRIS (Orsay, France). This work was

supported by the Italian Ministero dell'Istruzione, dell' Università e della Ricerca (MIUR) through the "Programma di Ricerca di rilevante Interesse Nazionale" (PRIN) Grant 2010C4R8M8_002 entitled "Nanoscale Functional Organization of (bio)Molecules and Hybrids for Targeted Application in Sensing, Medicine and Biotechnology" and the "Futuro in Ricerca" (FIRB) Grant RBFR1248UI 002 entitled "Novel Multiscale Theorethical/Computational Strategies for the Design of Photo and Thermo Responsive Hybrid Organic-Inorganic Components for Nanoelectronic Circuits".

Supporting Information. B3LYP intramolecular parameters of the gas-phase enol **OPr** obtained with different basis-sets; B3LYP-D* results for the main structural enol parameters; molecular atomic labelling and intermolecular interactions of the keto cluster; all frontier orbitals of gas-phase tautomers, solvated ones and clusters.

References:

1. Singer KD, Lalama SL, Sohn JE, Small RD (1987) Chapter II-8 - Electro-Optic Organic Materials. In: Zyss DSC (ed) Nonlinear Opt. Prop. Org. Mol. Cryst. Academic Press, pp 437–468

2. Ramamurthy V (1991) Photochemistry in organized and constrained media. Wiley-VCH, New York

3. Crano JC, Guglielmetti RJ (1999) Organic Photochromic and Thermochromic Compounds. Plenum Press, New York

4. Irie M (2000) Diarylethenes for memories and switches. Chem Rev 100:1685–1716. doi: 10.1021/cr980069d

5. Dürr H, Bouas-Laurent H (2003) Photochromism: Molecules and Systems, 2nd ed. Elsevier, Amsterdam

6. Sakai K, Kawamura H, Kobayashi N, et al. (2014) Highly efficient solid-state red fluorophores using ESIPT: crystal packing and fluorescence properties of alkoxy-substituted dibenzothiazolylphenols. CrystEngComm 16:3180–3185. doi: 10.1039/C3CE42109K

7. Kasha M (1963) Energy Transfer Mechanisms and the Molecular Exciton Model for Molecular Aggregates. Radiat Res 20:55–70. doi: 10.2307/3571331

8. Presti D, Labat F, Pedone A, et al. (2014) Computational Protocol for Modeling Thermochromic Molecular Crystals: Salicylidene Aniline As a Case Study. J Chem Theory Comput 10:5577–5585. doi: 10.1021/ct500868s

9. Mutai T, Satou H, Araki K (2005) Reproducible on–off switching of solid-state luminescence by controlling molecular packing through heat-mode interconversion. Nat Mater 4:685–687. doi: 10.1038/nmat1454

10. Harada J, Fujiwara T, Ogawa K (2007) Crucial Role of Fluorescence in the Solid-State Thermochromism of Salicylideneanilines. J Am Chem Soc 129:16216–16221. doi: 10.1021/ja076635g

11. Chung JW, You Y, Huh HS, et al. (2009) Shear- and UV-Induced Fluorescence Switching in Stilbenic π-Dimer Crystals Powered by Reversible [2 + 2] Cycloaddition. J Am Chem Soc 131:8163–8172. doi: 10.1021/ja900803d

12. Hongo K, Watson MA, Sánchez-Carrera RS, et al. (2010) Failure of Conventional Density Functionals for the Prediction of Molecular Crystal Polymorphism: A Quantum Monte Carlo Study. J Phys Chem Lett 1:1789–1794. doi: 10.1021/jz100418p

13. Pedone A, Presti D, Menziani MC (2012) On the ability of periodic dispersion-corrected DFT calculations to predict molecular crystal polymorphism in para-diiodobenzene. Chem Phys Lett 541:12–15. doi: 10.1016/j.cplett.2012.05.049

14. Kronik L, Tkatchenko A (2014) Understanding Molecular Crystals with Dispersion-Inclusive Density Functional Theory: Pairwise Corrections and Beyond. Acc Chem Res 47:3208–3216. doi: 10.1021/ar500144s

15. Grimme S (2006) Semiempirical GGA-type density functional constructed with a long-range dispersion correction. J Comput Chem 27:1787–1799. doi: 10.1002/jcc.20495

16. Civalleri B, Zicovich-Wilson CM, Valenzano L, Ugliengo P (2008) B3LYP augmented with an empirical dispersion term (B3LYP-D*) as applied to molecular crystals. Crystengcomm 10:405–410. doi: 10.1039/b715018k

17. Svensson M, Humbel S, Froese RDJ, et al. (1996) ONIOM: A Multilayered Integrated MO + MM Method for Geometry Optimizations and Single Point Energy Predictions. A Test for Diels−Alder Reactions and Pt(P(t-Bu)3)2 + H2 Oxidative Addition. J Phys Chem 100:19357–19363. doi: 10.1021/jp962071j

18. Vreven T, Morokuma K (2000) The ONIOM (our own N-layered integrated molecular orbital + molecular mechanics) method for the first singlet excited (S1) state photoisomerization path of a retinal protonated Schiff base. J Chem Phys 113:2969–2975. doi: 10.1063/1.1287059

19. Stephens PJ, Devlin FJ, Chabalowski CF, Frisch MJ (1994) Ab Initio Calculation of Vibrational Absorption and Circular Dichroism Spectra Using Density Functional Force Fields. J Phys Chem 98:11623–11627. doi: 10.1021/j100096a001

20. Dovesi R, Orlando R, Civalleri B, et al. (2005) CRYSTAL: a computational tool for the ab initio study of the electronic properties of crystals. Z Krist 220:571–573. doi: 10.1524/zkri.220.5.571.65065

21. R. Dovesi, V. R. Saunders, C. Roetti, et al. (2010) CRYSTAL09 User's Manual. Università di Torino, Torino

22. Presti D, Pedone A, Menziani MC, et al. (2014) Oxalyl dihydrazide polymorphism: a periodic dispersion-corrected DFT and MP2 investigation. Crystengcomm 16:102–109. doi: 10.1039/c3ce41758a

23. Presti D, Pedone A, Menziani MC (2014) Unraveling the Polymorphism of [(p-cymene)Ru(κN-INA)Cl2] through Dispersion-Corrected DFT and NMR GIPAW Calculations. Inorg Chem 53:7926–7935. doi: 10.1021/ic5006743

24. Hariharan PC, Pople JA (1973) The influence of polarization functions on molecular orbital hydrogenation energies. Theor Chim Acta 28:213–222. doi: 10.1007/BF00533485

25. Gill PMW, Johnson BG, Pople JA, Frisch MJ (1992) The performance of the Becke—Lee—Yang—Parr (B—LYP) density functional theory with various basis sets. Chem Phys Lett 197:499–505. doi: 10.1016/0009-2614(92)85807-M

26. Cossi M, Rega N, Scalmani G, Barone V (2003) Energies, structures, and electronic properties of molecules in solution with the C-PCM solvation model. J Comput Chem 24:669–681. doi: 10.1002/jcc.10189

27. M. J. Frisch, G. W. Trucks, H. B. Schlegel, G. E. Scuseria, M. A. Robb, J. R. Cheeseman, G. Scalmani, V. Barone, B. Mennucci, G. A. Petersson, H. Nakatsuji, M. Caricato, X. Li, H. P. Hratchian, A. F. Izmaylov, J. Bloino, G. Zheng, J. L. Sonnenberg, W. Liang, M. Hada, M. Ehara, K. Toyota, R. Fukuda, J. Hasegawa, M. Ishida, T. Nakajima, Y. Honda, O. Kitao, H. Nakai, T. Vreven, J. A. Montgomery, Jr., J. E. Peralta, F. Ogliaro, M. Bearpark, J. J. Heyd, E. Brothers, K. N. Kudin, V. N. Staroverov, T. Keith, R. Kobayashi, J. Normand, K. Raghavachari, A. Rendell, J. C. Burant, S. S. Iyengar, J. Tomasi, M. Cossi, N. Rega, J. M. Millam, M. Klene, J. E. Knox, J. B. Cross, V. Bakken, C. Adamo, J. Jaramillo, R. Gomperts, R. E. Stratmann, O. Yazyev, A. J. Austin, R. Cammi, C. Pomelli, J. W. Ochterski, R. L. Martin, K. Morokuma, V. G. Zakrzewski, G. A. Voth, P. Salvador, J. J. Dannenberg, S. Dapprich, P. V. Parandekar, N. J. Mayhall, A. D. Daniels, O. Farkas, J. B. Foresman, J. V. Ortiz, J. Cioslowski, and D. J. Fox (2009) GAUSSIAN09, Revision D.01. Gaussian, Inc., Wallingford CT

28. Mulliken RS (1955) Electronic Population Analysis on LCAO–MO Molecular Wave Functions. I. J Chem Phys 23:1833–1840. doi: 10.1063/1.1740588

29. Marenich AV, Jerome SV, Cramer CJ, Truhlar DG (2012) Charge Model 5: An Extension of Hirshfeld Population Analysis for the Accurate Description of Molecular Interactions in Gaseous and Condensed Phases. J Chem Theory Comput 8:527–541. doi: 10.1021/ct200866d

30. Bayly CI, Cieplak P, Cornell W, Kollman PA (1993) A well-behaved electrostatic potential based method using charge restraints for deriving atomic charges: the RESP model. J Phys Chem 97:10269–10280. doi: 10.1021/j100142a004

31. Singh UC, Kollman PA (1984) An approach to computing electrostatic charges for molecules. J Comput Chem 5:129–145. doi: 10.1002/jcc.540050204

32. Rappe AK, Goddard WA (1991) Charge equilibration for molecular dynamics simulations. J Phys Chem 95:3358–3363. doi: 10.1021/j100161a070

33. Martin F, Zipse H (2005) Charge distribution in the water molecule—A comparison of methods. J Comput Chem 26:97–105. doi: 10.1002/jcc.20157

Table 1. Optimized (B3LYP-D*) cell parameters and deviations relative to experiment, in parentheses (in Å, degrees and $Å^3$). For the keto form, deviations are calculated with respect to the enol form. The Relative Deviation % (RD %) is reported for the cell volume. The relative stability computed at ground state ($\Delta E = E_{keto} - E_{enol}$, in kcal/mol) is also reported.

	OPr enol (dev.)		**OPr** keto (dev.)		Exp. **OPr** enol[a]
a	11.531	(-0.199)	11.483	(-0.048)	11.730
b	22.140	(-0.148)	21.970	(-0.170)	22.288
c	7.286	(-0.194)	7.299	(+0.013)	7.480
β	98.762	(-1.676)	98.186	(-0.576)	100.438
Volume (RD %)	1838.46	(-4.40)	1822.60	(-0.86)	1923.10
	Relative Stability				
$\mathbf{E_{keto} - E_{enol}}$	+19.745	*per cell*			
	+4.936	*per molecule*			

a: from Ref.[6]

Table 2. Comparison of selected *inter*molecular distances (in Å). Deviations (in parentheses) of cluster parameters are reported with respect to the two corresponding crystalline forms.

	B3LYP				**Crystals B3LYP-D***	
	C-OPr-Enol		C-OPr-Keto		Enol	Keto
C16···H(a')	2.743	(0.008)	3.542	(-0.044)	2.735	3.586
H(a)···C16	2.735	(0.000)	3.578	(-0.008)	2.735	3.586
S2···H(b)	2.782	(-0.011)	2.883	(-0.003)	2.793	2.886
O1···H(c)	2.325	(-0.058)	2.265	(-0.015)	2.383	2.280
O2···H(d)	2.879	(0.018)	2.967	(0.004)	2.861	2.963
π···π	3.647	(0.004)	3.650	(0.000)	3.643	3.650

Table 3. Selected intra- and intermolecular parameters (in Å) computed at the ground (S_0) and first excited (S_1) states for the keto tautomer in gas-phase, solvent and clusters.

KETO	**Gas S_0**	**Gas S_1**	**$CHCl_3$ S_0**	**$CHCl_3$ S_1**	**Cluster S_0**	**Cluster S_1**
S1–C1	1.765	1.764	1.759	1.761	1.751	1.749
N1–C1	1.343	1.362	1.341	1.363	1.338	1.354
C2–C3	1.398	1.406	1.398	1.405	1.396	1.404
S1–C7	1.769	1.773	1.768	1.768	1.762	1.768
O1–C13	1.278	1.278	1.279	1.270	1.284	1.285
C8–C13	1.456	1.462	1.454	1.475	1.448	1.455
O2–C10	1.368	1.365	1.368	1.355	1.365	1.363
C1–C8	1.412	1.437	1.419	1.432	1.416	1.449
N1···O1	2.474	2.593	2.514	2.628	2.492	2.610
O1···H	1.531	1.746	1.615	1.833	1.555	1.768
H–N1	1.075	1.039	1.055	1.028	1.073	1.038
N1–H–O1	142.7	135.7	139.7	131.3	142.4	135.4
Intermolecular distances						
C16···H(a')					3.542	3.581
H(a)···C16					3.578	3.613
S2···H(b)					2.883	2.870
O1···H(c)					2.265	2.208
O2···H(d)					2.967	3.043
π···π					3.650	3.642

Table 4. Computed main vertical excitations and emission compared with experimental data, when available. 'H-L' stands for HOMO-LUMO. Energies in nm, oscillator strengths in a.u.

	Form	Character	λ_{max}	Osc. strength
Gas-phase	enol	H-L 0.70	403.42	0.37
	keto	H-L 0.70	586.85	0.34
$CHCl_3$	enol	H-L 0.70	406.50	0.53
	Exp. absorption[a]		390	
	keto	H-L 0.70	590.57	0.65
	Exp. emission[a]		619	
Clusters				
B3LYP/HF No EE	C-OPr-enol	H-L 0.70	402.15	0.37
B3LYP/MM EE Mulliken (HF/STO-3G)		H-L 0.70	393.35	0.40
B3LYP/MM EE RESP (HF/STO-3G)		H-L 0.70	393.73	0.38
B3LYP/MM EE RESP (HF/6-31G(d))		H-L 0.70	396.27	0.37
B3LYP/MM EE CM5 (HF/6-31G(d))		H-L 0.70	393.60	0.39
B3LYP/MM EE Q_{Eq}		H-L 0.70	403.35	0.33
	Exp. Fluo. Excitation Crystal[a]		438	
B3LYP/HF No EE	C-OPr-keto	H-L 0.71	605.46	0.31
B3LYP/MM EE Mulliken (HF/STO-3G)		H-L 0.71	562.90	0.35
B3LYP/MM EE RESP (HF/STO-3G)		H-L 0.71	580.62	0.33
B3LYP/MM EE RESP (HF/6-31G(d))		H-L 0.71	580.20	0.33
B3LYP/MM EE CM5 (HF/6-31G(d))		H-L 0.71	579.11	0.32
B3LYP/MM EE Q_{Eq}		H-L 0.71	629.53	0.27
	Exp. Fluo. Emission Crystal[a]		589	

a: from Ref.[6]

Table 5. Computed Stokes' shifts for the cluster moieties vs. experiment.

Approach	Stokes' shift (nm)
B3LYP/HF No EE	203
B3LYP/MM EE Mulliken (HF/STO-3G)	170
B3LYP/MM EE RESP (HF/STO-3G)	187
B3LYP/MM EE RESP (HF/6-31G(d))	184
B3LYP/MM EE CM5 (HF/6-31G(d))	185
B3LYP/MM EE Q_{Eq}	226
Exp.	151

CAPTIONS TO FIGURES

Figure 1. Scheme of the ESIPT process that takes place for **OPr**.

Figure 2. View (*ab* plane) of the fully optimized **a)** enol and **b)** keto ground state crystalline forms of **OPr**. Intramolecular hydrogen bonds are displayed in enhanced views. The unit cell, containing four symmetry-equivalent molecules, is highlighted in violet.

Figure 3. (Top left) Perspective and (Top right) top view of the optimized **C-OPr-enol** cluster; the central molecule is highlighted in red. (Bottom) Labeling of selected intermolecular distances is given.

Figure 4. Difference between distances of selected intra- and intermolecular parameters for the **OPr** keto tautomer computed at the excited (S_1) and ground (S_0) states.

Figure 5. Spectra computed for the enol (absorption, continuous lines) and keto (emission, dashed lines) tautomers of **OPr** in gas-phase and in solution (chloroform). The spectra obtained from QM/MM embedded cluster calculations (HF/STO-3G Mulliken charges in the low level region) are also reported.

Figure 6. Frontier orbitals derived from embedded cluster calculations of **OPr**, computed at B3LYP/MM EE (Mulliken) (right) and B3LYP/MM EE (CM5) (left) levels.

Figure 7. UV-Visible spectra computed for the **C-OPr-enol** (absorption, continuous lines) and **C-OPr-keto** (emission, dashed lines) clusters, obtained by using different charge embedding protocols. The inset shows an enhanced view of the absorption region.

FIGURE 1

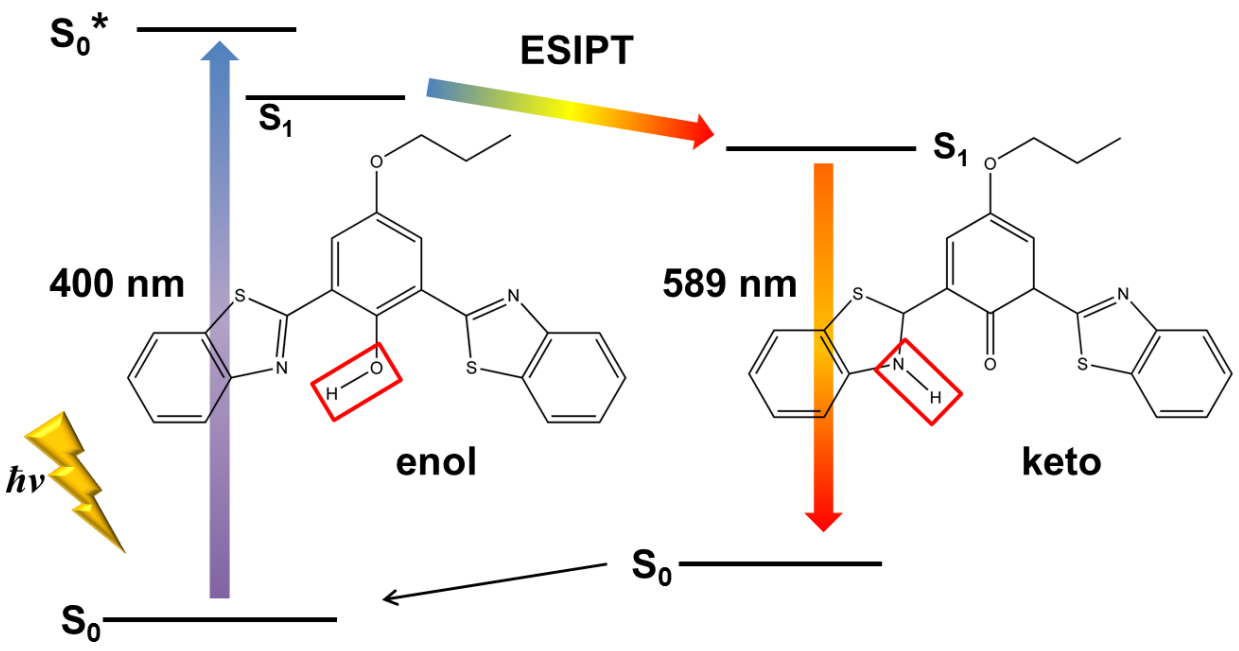

FIGURE 2

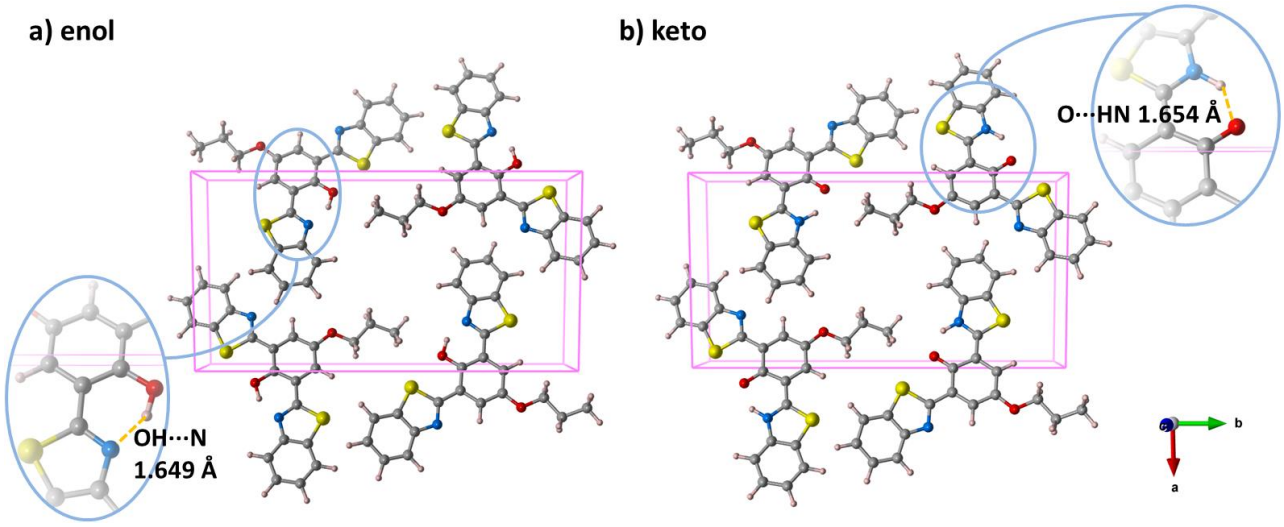

FIGURE 3

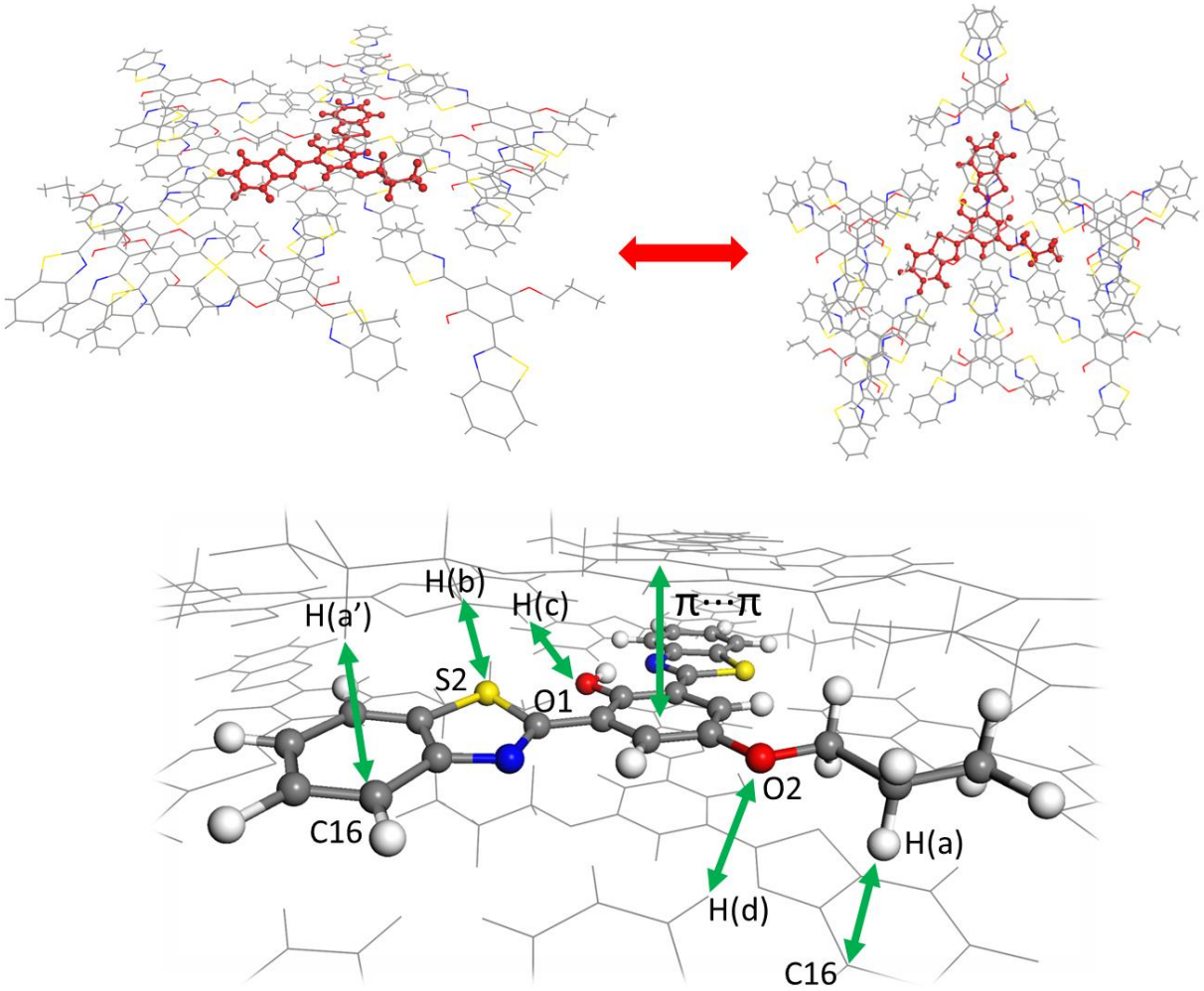

FIGURE 4

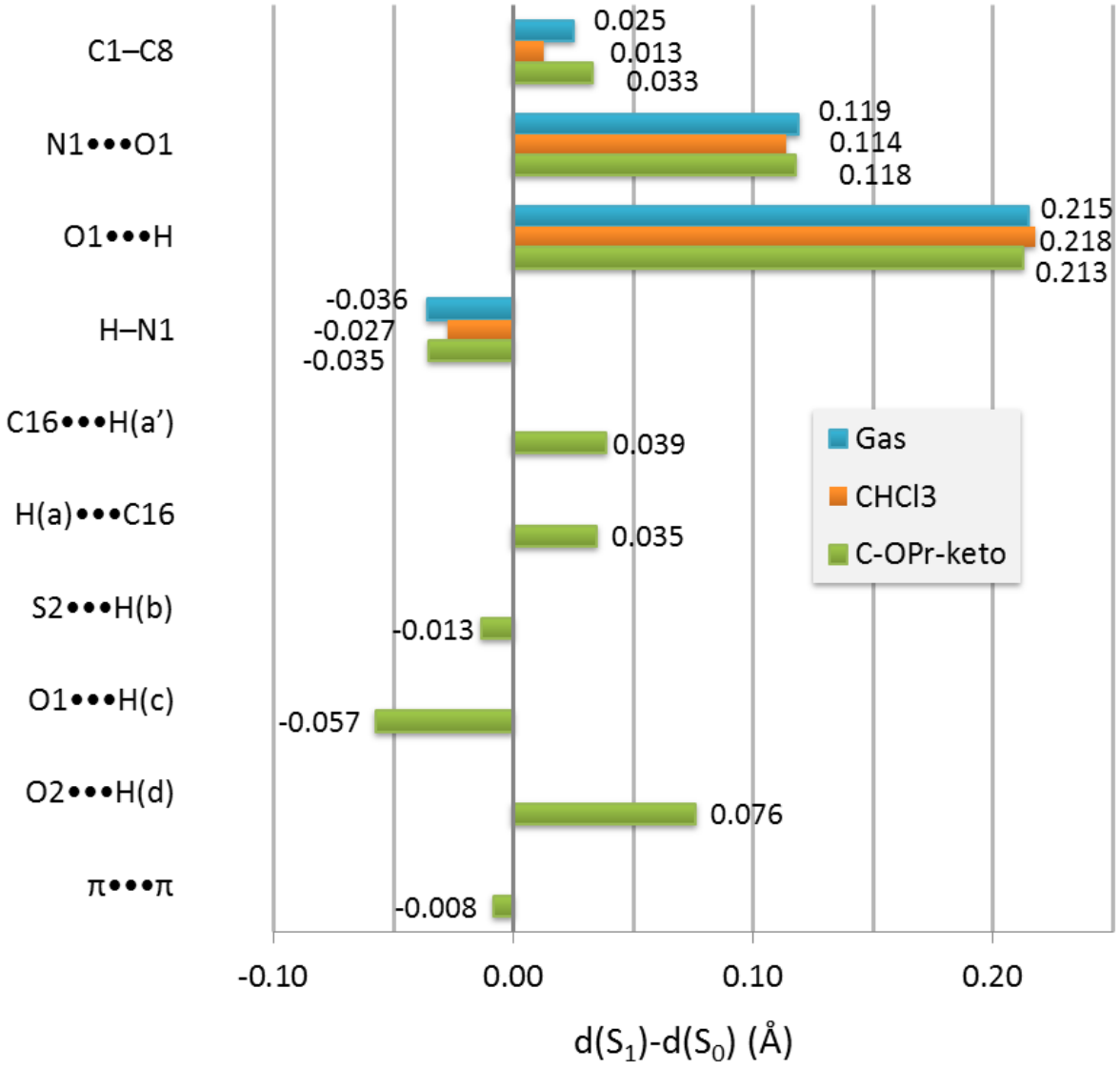
C1–C8
N1•••O1
O1•••H
H–N1
C16•••H(a')
H(a)•••C16
S2•••H(b)
O1•••H(c)
O2•••H(d)
π•••π
0.025
0.013
0.033
0.119
0.114
0.118
0.215
0.218
0.213
-0.036
-0.027
-0.035
0.039
0.035
-0.013
-0.057
0.076
-0.008
Gas
CHCl3
C-OPr-keto
-0.10
0.00
0.10
0.20
d(S1)-d(S0) (Å)

FIGURE 5

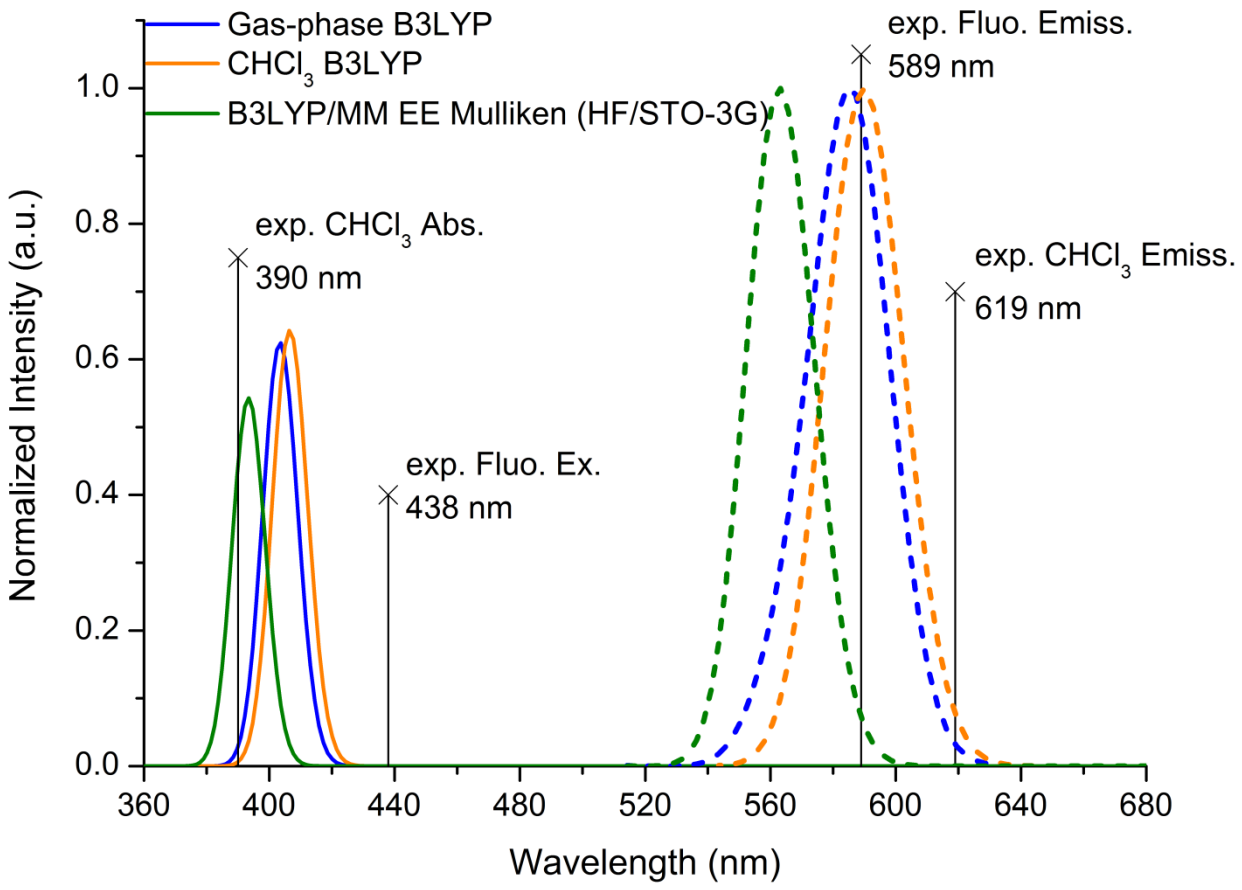
Gas-phase B3LYP
CHCl3 B3LYP
B3LYP/MM EE Mulliken (HF/STO-3G)
exp. Fluo. Emiss.
589 nm
exp. CHCl3 Abs.
390 nm
exp. CHCl3 Emiss.
619 nm
exp. Fluo. Ex.
438 nm
Normalized Intensity (a.u.)
Wavelength (nm)
0.0
0.2
0.4
0.6
0.8
1.0
360
400
440
480
520
560
600
640
680

FIGURE 6

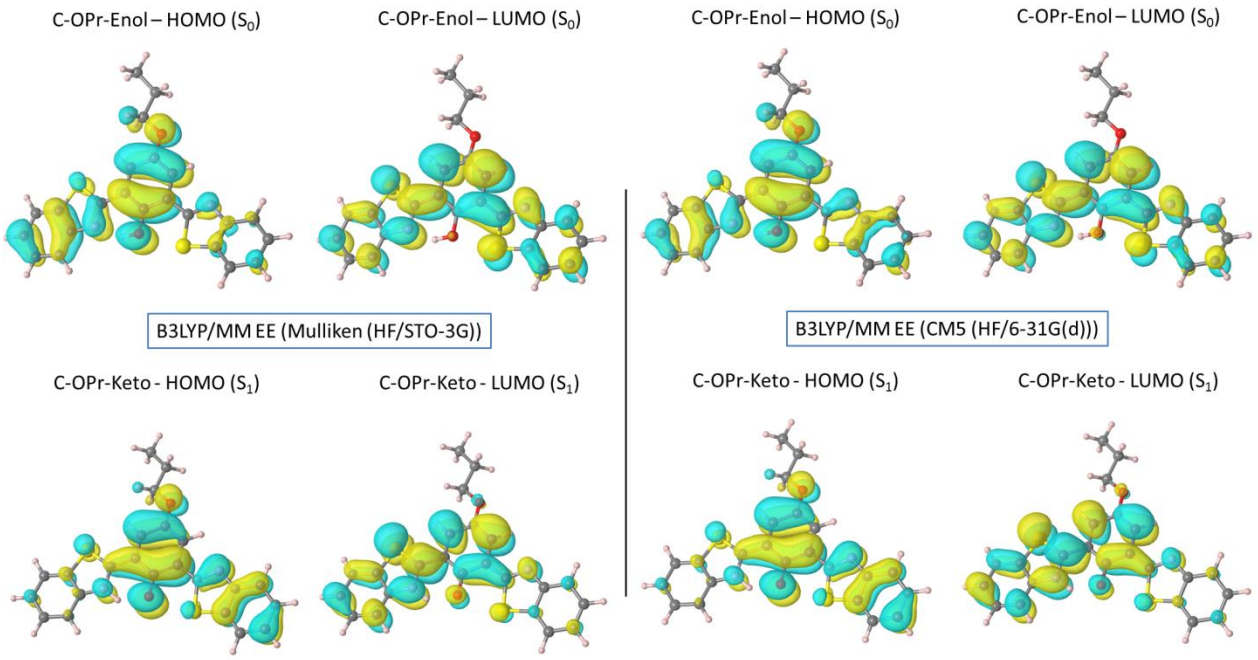
C-OPr-Enol – HOMO (S_0)
C-OPr-Enol – LUMO (S_0)
C-OPr-Enol – HOMO (S_0)
C-OPr-Enol – LUMO (S_0)
B3LYP/MM EE (Mulliken (HF/STO-3G))
B3LYP/MM EE (CM5 (HF/6-31G(d)))
C-OPr-Keto - HOMO (S_1)
C-OPr-Keto - LUMO (S_1)
C-OPr-Keto - HOMO (S_1)
C-OPr-Keto - LUMO (S_1)

FIGURE 7

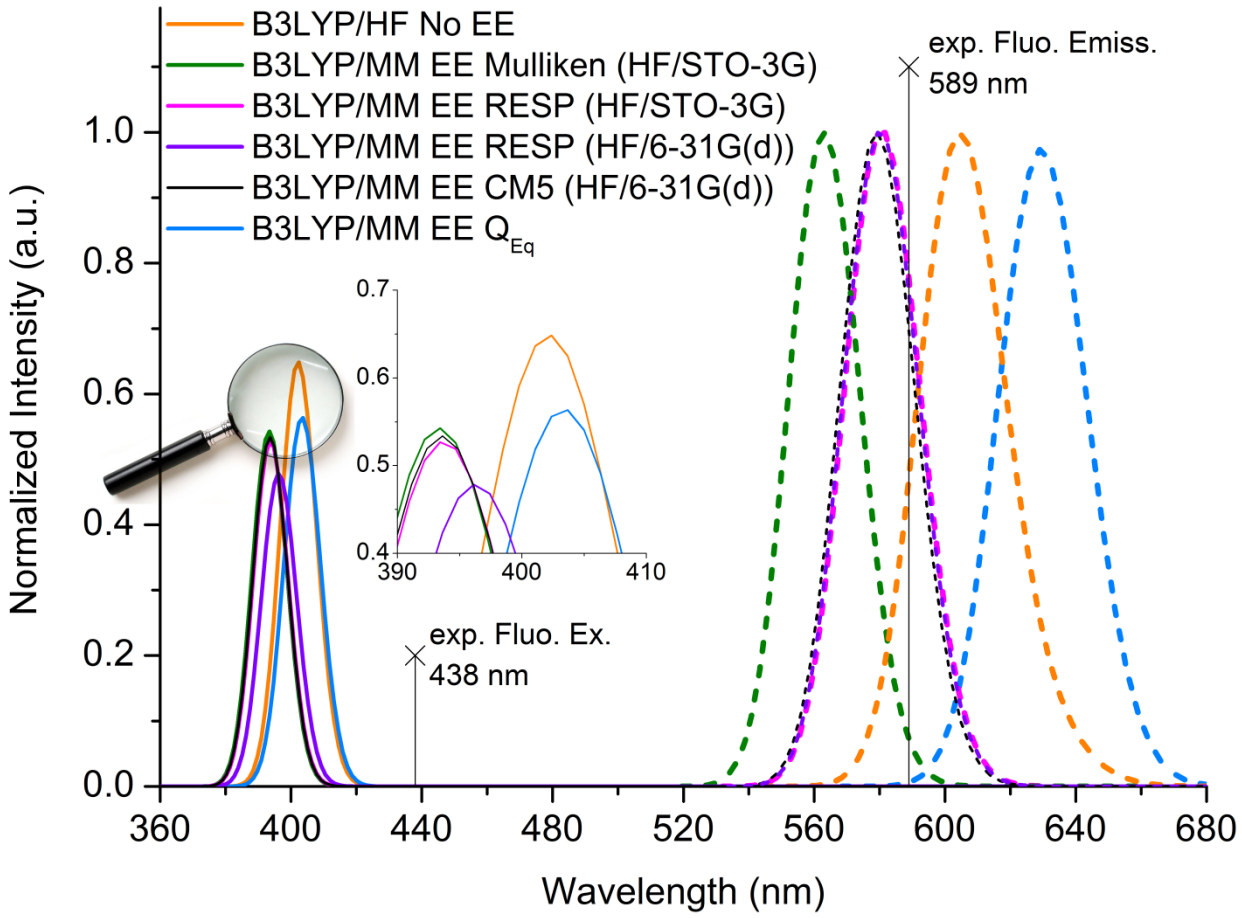
B3LYP/HF No EE
B3LYP/MM EE Mulliken (HF/STO-3G)
B3LYP/MM EE RESP (HF/STO-3G)
B3LYP/MM EE RESP (HF/6-31G(d))
B3LYP/MM EE CM5 (HF/6-31G(d))
B3LYP/MM EE Q$_{Eq}$
exp. Fluo. Emiss.
589 nm
exp. Fluo. Ex.
438 nm
Normalized Intensity (a.u.)
Wavelength (nm)
0.0
0.2
0.4
0.6
0.8
1.0
360
400
440
480
520
560
600
640
680
0.4
0.5
0.6
0.7
390
400
410